PACS:61.43.Gt; 68.03.-g; 68.43.-h; 81.40.Ef doi: 10.15407/Surface.2023.15.080

POROSITY AND PACKING FEATURES OF NANO- AND MICRO-PARTICLES OF CARBON AND SILICA ADSORBENTS

V.M. Gun'ko

Chuiko Institute of Surface Chemistry, 17 General Naumov Street, 03164 Kyiv, Ukraine
e-mail: vlad_gunko@ukr.net

Comparative characterization of the particulate morphology and texture of various silicas (fumed silicas, silica gels, ordered mesoporous silicas) and carbons (chars and activated carbons, AC) is of interest from both theoretical and practical points of view since it allows one better understanding of advantages and disadvantages of various adsorbents upon their interactions with different adsorbates, co-adsorbates, and solutes in various dispersion media. Complete characterization needs application of a certain set of methods that is analyzed in the present paper. It is shown that the main difference in the textural characteristics of silica and carbon adsorbents is due to the absence (silicas) or presence (carbons) of nanopores in nanoparticles (NP). A great contribution of these pores in strongly activated carbons provides the specific surface area values greater by an order of magnitude than that of fumed silicas. Despite a high activation degree of AC, contribution of closed pores or pores inaccessible for nitrogen molecules remains relatively large in contrast to fumed silica A–300 composed of nonporous nanoparticles synthesized in the flame at higher temperature (~80% of melting temperature, T_m, for amorphous silica) than carbon activation temperature (~25%of T_m for carbons). Therefore, the pores inaccessible for nitrogen molecules in fumed silica could be attributed to narrow voids around contact area between neighboring NP in their aggregates, but for AC, there are both closed pores and open nanopores inaccessible for nitrogen molecules. For complete characterization of the morphology and texture of various adsorbents, such methods as transmission and scanning electron microscopies, probe (nitrogen, argon) adsorption, smallangle X-ray scattering (SAXS)and X-ray diffraction (XRD)could be used with appropriate software to analyze the data. The latter is especially important for the analyses of indirect data (e.g., adsorption, SAXS, XRD) characterizing the materials.

Keywords*: fumed nanosilicas; porous silicas; carbon adsorbents; particulate morphology; nanoparticle porosity; textural characteristics*

Introduction

The specific surface area (SSA), pore size distribution (PSD), and pore volume are the main characteristics of any adsorbent [1–6]. These characteristics depend strongly on the porosity and packing feature of nanoparticles (NP) as the main structural elements of adsorbents with relatively great SSA and porosity [5–18]. As a whole, there are two main kinds of adsorbents composed of porous (PNP) and nonporous (NPNP) nanoparticles forming secondary porous structures. For example, chars and activated carbons (AC) belong to the first kind of adsorbents with PNP and their porosity is provided by pores in both PNP and secondary structures such as aggregates of NP and microparticles formed by NP aggregates [7–9].Fumed nanosilicas, silica gels, and ordered mesoporous silicas correspond to the second kind of

adsorbents with NPNP, *i.e*., only secondary structures are responsible for the porosity of these materials and the porosity is attributed to textural one [10–19].

The particulate morphology and texture of adsorbents are characterized by a certain hierarchy with several steps such as (i) individual and stacked sheets, clusters, graphenes packed in porous carbon nanoparticles (5–50 nm in size) tightly aggregated (aggregate size < 1 μm as conventional limit size) by chemical bondingin microparticles (agglomerates, globules) of AC [7–9]; (ii) nanosilica nuclei tightly packed in NPNP loosely binding in aggregates (mainly by electrostatic and van-der-Waals forces) forming agglomerates (1–50 μm in size) of aggregates ("soft" supra-NP structures) and visible light soft particles composed of supra-NP structures of fumed silicas [12–19]. For some nanosilicas, rigid primary aggregates of 50–100 nm in size could be formed in the flame due to the formation of certain chemical bonds between neighboring NP. Note that these rigid aggregates could remain in treated aqueous suspensions, mechano-activated wetted powders, *etc*., in contrast to larger supra-NP structures [16, 17]. Silica gels, precipitated silicas, ordered mesoporous silicas,and some other porous silicas are composed of NPNP more densely and tightly packed in rigid secondary structures (micro- or macro-particles, globules) than NPNP in supra-NP structures of fumed silicas [10–19].

The morphological and textural hierarchies strongly affect the adsorption capacity of adsorbents with respect to low- and high-molecular weight adsorbates [4–17]. For example, light gases (H_2, CH_4) could be poorly adsorbed in broad pores and onto outer surface of NPNP and well adsorbed in nanopores in PNP, but polymers (especially 3D branched ones) cannot be adsorbed in nanopores and narrow mesopores in contrast to light gases. Therefore, the light gases adsorption depends mainly on the textural characteristics (PNP *vs*. NPNP),and it is practically independent of the supra-NP morphology (*i.e*., aggregation of NP in the secondary structures), but the adsorption of high-molecular weight compounds (polymers, proteins, *etc*.) is strongly governed by the supra-NP morphology (particle size distributions, PaSD and their aggregation features in supra-NP structures). As a consequence, proteins much better adsorb (this is rather agglutination of macromolecules with NP than simple adsorption) onto fumed silicas than onto AC, but hydrogen and methane well adsorb onto nanoporous AC and do not practically adsorb onto fumed silicas [16, 19]. However, there is a small number of publications related to comparative elucidation of the effects of porosity and packing features of NP in different adsorbents such as carbons and silicas. Therefore, the aim of this work was to show some general features of the morphology and texture of AC, nanosilicas, porous silica gels,and ordered mesoporous silica (that affect the adsorption capacity of these materials)comparatively analyzed using transmission (TEM) and scanning(SEM) electron microscopy, atomic force microscopy (AFM), nitrogen adsorption, SAXS, and XRD methods with accurate computations of the characteristics with developed software based on simple and self-consistent regularization procedures previously applied to different materials [20–29].

They are characterized by different morphology, texture, and structure: (i) commercial silica gels HP39 and Gasil 200DF (Cros field); (ii) fumed silicas A–300 and A–500 synthesized in the $H_2/O_2/N_2$ flame (1400–1500 K) using $SiCl_4$ as a precursor (Pilot plant, Chuiko Institute of Surface Chemistry (CISC), Kalush, Ukraine); (iii) ordered mesoporous silica MCM–41 (CISC) [16]; and (iv) char (C–0) and activated carbons (AC) C–30, C–45, C–60, and C–86(series C–*x*) with the burn-off degree of 30, 45, 60, and 86 %, respectively, synthesized using phenolformaldehyde resin carbonized in the CO_2 atmosphere at elevating temperature from ambient to 1073 K at a heating rate of 3 K/min and then activated by CO_2 at 1173 K during different time to provide various burn-off degree(MAST Carbon International Ltd., UK) [16, 30, 31]. Several nanoporous AC synthesized using various natural raw materials (plum stones, coconut shells, woodchips)[16] were used for certain comparison with C–*x* AC.

Materials

Various materials were selected as representatives of silica and carbon adsorbents (Table 1).

Table 1. Textural characteristics of various adsorbents studied

Sample	S_{BET} m^2/g	S_{nano} m^2/g	S_{meso} m^2/g	S_{macro} m^2/g	S_{NLDFT} m^2/g	V_p cm^3/g	V_{nano} cm^3/g	V_{meso} cm^3/g	V_{macro}, cm^3/g	$<R_V>$ nm	$<R_S>$ nm
200DF	540	429	111	0.0	496	0.336	0.244	0.092	0.0	0.92	0.87
HP–39	448	175	272	0.0	446	1.824	0.129	1.695	0.0	9.07	4.62
MCM–41	788	234	554	0.5	682	0.604	0.076	0.513	0.015	3.22	1.50
A–500	492	238	237	17	489	0.874	0.055	0.583	0.236	20.47	5.22
A–300	294	44	229	16	291	0.850	0.023	0.567	0.259	20.41	6.14
C–0	537	454	68	14	673	0.829	0.158	0.477	0.195	17.10	2.76
C–30	1074	905	161	8	1284	1.292	0.355	0.713	0.224	16.38	1.77
C–45	1615	1456	148	11	1783	1.319	0.563	0.452	0.304	17.91	1.25
C–60	1999	1750	242	8	2201	1.969	0.822	0.950	0.197	9.50	1.31
C–86	3463	3104	354	5	2800	2.320	1.473	0.644	0.204	8.31	0.89

Note.V_{nano}, S_{nano}, V_{meso}, S_{meso}, V_{macro} and S_{macro} were calculated by $f_V(R)$ and $f_S(R)$ integration at 0.35 nm<R<1 nm, 1 nm<R<25 nm, and 25 nm<R<100 nm, respectively; average pore radii $<R_V>$ and $<R_S>$ were calculated as a ratio of the first/zero moments $<R>=\int f(R)RdR/\int f(R)dR$ with respect to the pore volume and surface area, respectively.

Transmission (TEM), scanning (SEM) electron and atomic force (AFM) microscopy

TEM images were recorded using a TECNAI G2 F30 microscope (FEI–Philips, Holland) and JEOL JEM–2100F (Japan) at an operating voltage of 300 kV. A dried sample was added to acetone (chromatographic grade) and sonicated to form uniform suspension. Then a suspension drop was deposited on a copper grid with a thin carbon film. After evaporation of acetone, nanostructured particles remained on the film were investigated.

SEM equipment (FE–SEM, Hitachi S–4700, Tokyo, Japan, operating voltage V = 15 kV, magnification of ×5000–100000; Quanta TM 3D FEG, FEI, USA, V = 5–30 kV; and Zeiss Gemini 300, Carl ZEISS,V = 0.02 – 30 kV) was used to analyze the morphology.

NanoScope III (Digital Instruments, USA) apparatus was used a tapping mode to record AFM images. Before AFM scanning, samples were slightly smoothed by hand pressing using a glass plate, which does not affect their structure.

SAXS

The differential pore size distribution (PSD) functions $f(r)$ based on the small-angle X-ray scattering (SAXS) [32–36] data were calculated using Fredholm integral equation of the first kind for scattering intensity $I(q)$ [32–34]

$$I(q) = C \int_{r_{min}}^{r_{max}} \frac{\left(\sin qr - qr\cos qr\right)^2}{(qr)^2} V(r) f(r) dr \,, \qquad (1)$$

where C is a constant, $q = 4\pi\sin(\theta)/\lambda$ the scattering vector value, 2θ is the scattering angle, λ is the wavelength of incident X-ray, $V(r)$ is the volume of a pore with radius r (proportional to r^3), and $f(r)dr$ represents the probability of having pores with radius r to $r + dr$. The values of $r_{min}(= \pi/q_{max})$ and r_{max} $(= \pi/q_{min})$ correspond to lower and upper limits of the resolvable real space due to instrument resolution. This equation was solved using the CONTIN algorithm [37]. The $f(r)$ function could be converted into incremental PSD (IPSD) $\Phi(r_i) = (f(r_{i+1}) + f_V(r_i))(r_{i+1} - r_i)/2$ for better view of the PSD at larger r values.

To calculate the particle size distribution (PaSD) functions, several models of particles (e.g., spherical, cylindrical, lamellar ones and various blends of them) could be used. For spherical particles, integral equation similar to Eq. (1) could be written as follows

$$I(q) = C \int_{R_{\min}}^{R_{\max}} P(q,R) f(R) dR\,, \tag{2}$$

where C is a constant, R is the radius of particles, $f(R)$ is the distribution function (differential PaSD), and $P(R)$ is the form factor for spherical particles (the kernel of the integral equation 2): $P(q,R) = (4\pi R^3/3)^2[\Phi(q)]^2$ and $\Phi(q,R) = (3/(qR)^3)[\sin(qR) - qR\cos(qR)]$.

The PaSD with respect to the volume of particles (as abundance in vol%) could be calculated as follows

$$\text{abundance(vol\%)} = R^3 f(R) / \int R^3 f(R) dR\,. \tag{3}$$

For cylindrical particles, there are two variable parameters, such as the radius (R) and length (H) of cylinders

$$I(q) = C \int_{H_{\min}}^{H_{\max}} \int_{R_{\min}}^{R_{\max}} f(H) f(R) P(q,H,R) dH dR\,, \tag{4}$$

where $P(q,H,R) = CV \int_0^{\pi/2} \frac{2J_1(qR\sin\theta)}{qR\sin\theta} \frac{\sin\left(0.5qH\cos\theta\right)}{0.5qH\cos\theta} \sin\theta d\theta$, $J_1(x)$ is the first-order Bessel function, $V = \pi R^2 H$ is the cylinder volume, and C is a constant.

For lamellar particles

$$I(q) = C \int_{L_{\min}}^{L_{\max}} P(q,L) f(L) dL\,, \tag{5}$$

where $P(q,L) = (L/q)^2 \left[\frac{\sin(qL/2)}{(qL/2)}\right]^2$, L is the lamellar thickness, and the prefactor ($1/q^2$) is the so-called Lorentz factor required to randomize the orientation of the lamellar particle. In the case of complex systems, several models with various blends of spherical, cylindrical and lamellar particles could be used with certain weight coefficients. For complex particles, a model includes spherical, cylindrical, and lamellar particles [26–29]

$$\begin{aligned} I(q) = {} & c_{sph} \int_{R_{\min}}^{R_{\max}} \left(\frac{4\pi R^3}{3}\right)^2 \left[\frac{3}{(qR)^3}(\sin(qR) - qr\cos(qR))\right]^2 f(R) dR + \\ & + c_{lam} \int_{L_{\min}}^{L_{\max}} (L/q)^2 \left[\frac{\sin(qL/2)}{(qL/2)}\right]^2 f(L) dL + \\ & + c_{cyl} \int_{H_{\min}}^{H_{\max}} f(H) \int_{R_{\min}}^{R_{\max}} \frac{\pi R^2}{H} f(R) \int_0^{\pi/2} \sin\theta \frac{2J_1(qR\sin\theta)}{qR\sin\theta} \frac{\sin\left(0.5qH\cos\theta\right)}{0.5qH\cos\theta} d\theta dR dH\,, \end{aligned} \tag{6}$$

where $I(q)$ is the X-ray scattering intensity, $q = 4\pi\sin(\theta)/\lambda$ is the scattering vector value, 2θ is the scattering angle, λ is the wavelength of incident X-ray, R is the radius of particles, H and R are the length and radius of cylinders, L is the lamellar thickness, $f(R)$, $f(L)$, and $f(H)$ are the

distribution functions, $J_1(x)$ is the first-order Bessel function, c_x are the weight coefficients calculated, as well $f(x)$ functions, using a self-consistent regularization procedure.

The specific surface area from the SAXS data could be estimated [32–36] (in m^2/g) using equation

$$S_{\text{SAXS}} = 10^4 \pi\phi(1-\phi)\frac{K}{Q\rho_a}, \tag{7}$$

where $\phi = \rho_a/\rho_0$ is the solid fraction of adsorbent, and Q is the invariant

$$Q = \int_0^\infty q^2 I(q)dq\,. \tag{8}$$

The Q value is sensitive to the range used on integration of Eq. (8) (since experimental q values are measured between the $q_{\min}$ and $q_{\max}$ values different from 0 and ∞). Therefore, the invariant value Q was calculated using equation [32–36]

$$Q = \sum_{q_{\min}}^{q_{\max}} (I(q_i) - b)q_i^2 \Delta q_i + K / q_{\max}, \tag{9}$$

where b is a constant determined using equation

$$I(q)q^4 = K + bq^4 \tag{10}$$

valid in the Porod range.

XRD

X-ray diffraction (XRD) patterns were recorded over 2θ = 1–10°(MCM–41) and 10–60° (A–300) range using DRON4-07 and DRON-3M diffractometers (LOMO and Bourevestnik, Inc., St. Petersburg) with Cu K_α (λ = 0.15418 nm) radiation and a Ni filter.The XRD data could be used for simple estimation of average sizes of crystallites ($d$cr) using Scherrer or Debye–Scherrer equations [38, 39]. The XRD data could be also used to estimate the crystallite size distribution (CSD) functions using full profile analysis of selected lines or total XRD patterns [40, 41]. To calculate the broadened line (pure) profile related to the crystallite size/faulting effects of materials studied, as well a size distribution function, one could use twointegral equations [40–42]:

$$\begin{aligned} I_{\text{ex.obs.}}(\varepsilon) &= C\int h_{e.p.}(\varepsilon - t)i_{ex.pure}(t)dt \\ i(s) &= \int_0^\infty D\frac{\sin^2(\pi sD)}{(\pi sD)^2}g(D)dD \end{aligned} \tag{11}$$

where $I_{ex.obs.}(\varepsilon)$ is the experimentally observed X-ray diffraction profile, C is a constant, $h_{\text{e.p.}}$ is the instrumental profile, $i(s)$ is the pure crystallite size/faulting profile, D is the crystallite size, $g(D)$ is the CSD function, 2θis the scattering angle, $2\theta_{hkl}$is the scattering angle corresponding to apeak [40]

$$s = s_{2\theta} - r^*_{hkl} = \frac{2\sin\theta}{\lambda} - \frac{2\sin\theta_{hkl}}{\lambda} \approx \frac{\cos\theta_{hkl}}{\lambda}(2\theta - 2\theta_{hkl}) \tag{12}$$

The variable ε in Eq. (11) corresponds to the angular deviation of a point from the true Bragg angle $2\theta_0$; and ε and the auxiliary variable t have the dimension of 2θ.

Textural characteristics

The textural characteristics of samples degassed at 453 K for 12 hours were studied using low–temperature (77.4 K) nitrogen adsorption–desorption isotherms (Micromeritics ASAP 2010, 2405N, or 2420 adsorption analyzer). The specific surface area (Table 1, S_{BET}) was calculated according to the BET method [1, 2]. The total pore volume (Table 1, V_p) was estimated from the adsorption at high relative pressure $p/p_0 \approx$ 0.98–0.99 [1,2]. The differential ($f_V(R) = dV/dR$) pore size distributions (PSD) were calculated using a nonlocal density functional theory (NLDFT, Quantachrome software) method with a model of cylindrical pores in silica and slit/cylindrical or slitshapedpores in carbons [43–47]. The incremental PSD (IPSD, $\Phi_V(R_i) = (f_V(R_{i+1}) + f_V(R_i))(R_{i+1} - R_i)/2$ at $\sum\Phi_V(R_i) = V_p$) were computed using a complex model of pores in silica (slit shaped and cylindrical pores and voids between nanoparticles, SCV model) with a self–consistent regularization (SCR) procedure (SCV/SCR method) and DFT method [27].

Results and discussion

Fumed silica, char, and AC are composed of nanoparticles loosely (nanosilica) or tightly (AC) aggregated in secondary structures (Figs. 1–3).SEM (Figs. 1e,f and 3b,c) and AFM (Fig. 3a,d) images give roughly similar pictures of aggregates in these nanostructured materials. However, TEM images (Figs. 1a–d and 2a–c) show the difference in the NP morphology of fumed silica and carbon adsorbents, *e.g.*, carbon NP are larger and porous, but silica NP are smaller and nonporous. Additionally, AC visible particles could represent relatively dense microglobules (Fig. 3), but nanosilica forms loose agglomerates (Fig. 2d) forming a light powder with very low bulk density (ρ_b). Typically, the ρ_b value of the initial fumed silica powders(0.04–0.06 g/cm^3 providing the empty volume up to $V_{em} = 1/\rho_b - 1/\rho_0$ = 24.5–16.2 cm^3/g, respectively, where $\rho_0 \approx$ 2.2 g/cm^3 is the true density of amorphous silica) is essentially smaller than the ρ_b value of AC (0.2–0.5 g/cm^3) despite theirρ_0 values are similar (2.0–2.2 g/cm^3).This difference is due to two main factors: (i) denser packing of carbon NP in aggregates and globules than silica NP in aggregates/agglomerates packing in loose visible particles (Figs. 1–3); and (ii) nanoporosity of carbon NP in contrast to nonporous NP of nanosilica (Figs. 4–8). The first factor leads to a larger difference in the ρ_b values of AC and nanosilica, but the second one gives the opposite result. Notice that after hydro-compaction of nanosilica (Fig. 2c) with wetting–stirring–drying, the ρ_b value increases up to 0.3–0.6 g/cm^3(dependent on treatment conditions) [16, 17, 29] giving the V_{em} values (2.9–1.2 cm^3/g, respectively) reduced to values similar to the pore volume of AC (Table 1, V_p).

In addition to the difference in the particulate morphology of AC and nanosilica, their main textural difference is due to NP (non)porosity since nanosilica is composed of NPNP, but carbons are composed of PNP. Very large SSA values of AC provide direct evidence of the carbon NP porosity, since SSA ~ 1/d and NPNP of A–500 ($d \approx$ 5.5 nm in the average diameter) much smaller than AC NP (Figs. 1–3) could provide only 14–46 % of the SSA values of AC studied (Table 1). Note that the main textural difference between chars and related AC is due to much larger contribution of closed pores in chars than in AC because the carbon activation (burn-off) leads to an increase of contribution of open pores with increasing the burn-off degree of AC. This is clear from comparison of the S_{SAXS} and S_{BET} values (Tables 1 and 2) and a characteristic increase in contribution of nanopores accessible for nitrogen molecules (Fig. 4b) in contrast to the SAXS PSD (Fig. 4a), which do not practically change in the range of nanopores (R< 1 nm) for AC (C–30, C–45, and C–60). As a whole, there is a tendency of broadening of nanopores and narrow mesopores (mainly pores in NP interior) in contrast to narrowing of main

mesopores (pores between neighboring NP at pore radius R = 5–25 nm) with increasing the burn-off degree of AC because AC NP become smaller due to burn-off (Fig. 4).

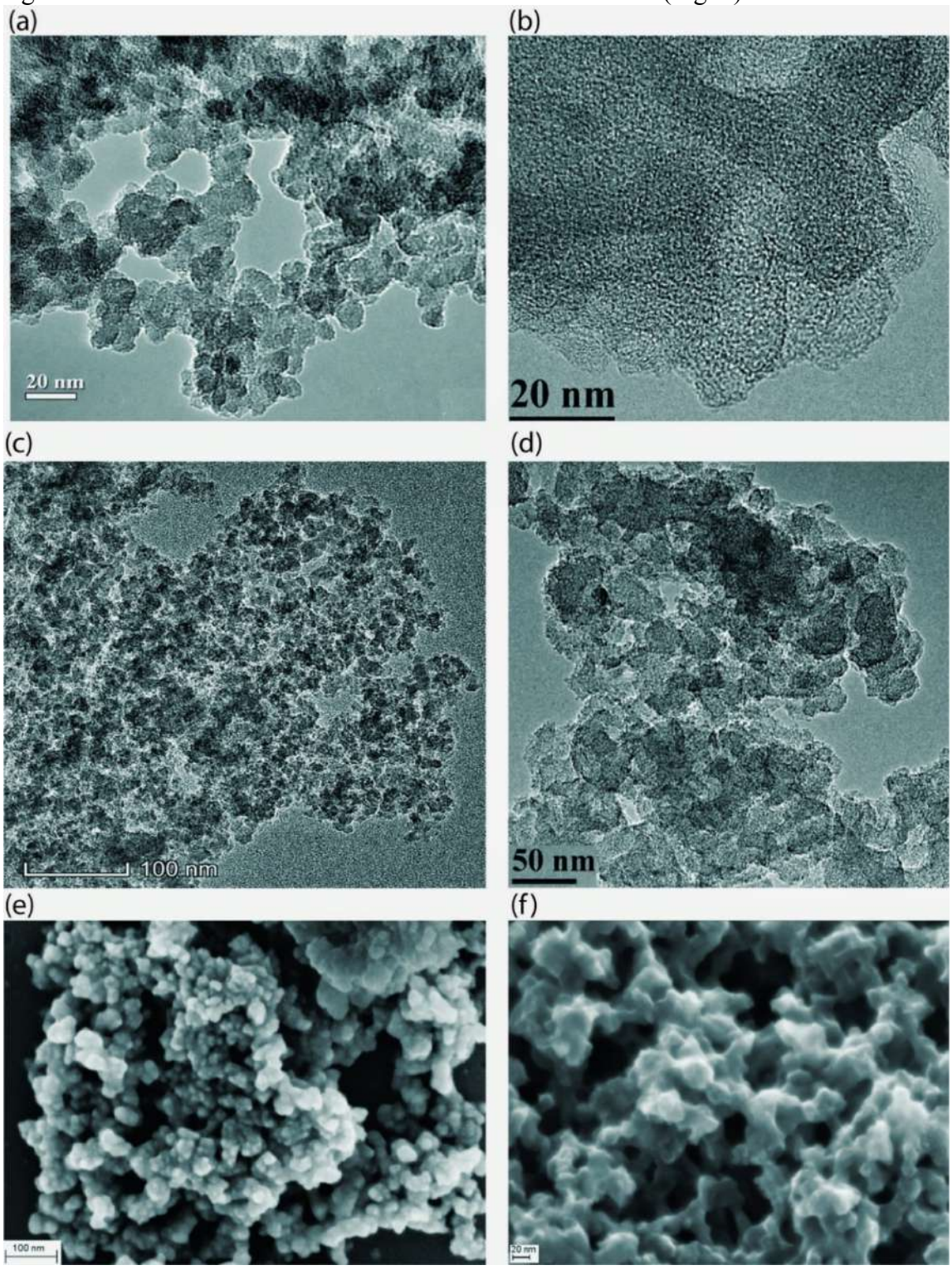

Fig. 1. TEM (a–d) and SEM (e, f) images of nanosilica A–300 (a, c, e) and carbons: charC–0 (b, d) and AC C–45 (f) (scale bar: 20 nm (a, b, f), 100 nm (c, e), and 50 nm (d))

Contribution of closed pores or pores inaccessible for nitrogen molecules could be estimated using the SAXS and adsorption data (Table 2). For fumed silica, it is small (about 7%) in contrast to C–0 (about 55%), but this contribution decreases with increasing the burn-off

degree. However, even for C–60 with SSA_{N2} of 45% of the theoretical SSA limit value, contribution of closed pores or pores inaccessible for nitrogen molecules remains relatively high (about 25%). This is due to high contribution of nanopores (Table 1, S_{nano}, V_{nano}) in relatively large PNP of AC. A part of these nanopores could be inaccessible for nitrogen molecules due to complex topology of them because of nonuniform location and size distribution of graphenes and graphene clusters, and their nonplanar shape in NP (Figs. 1 and 2, TEM images).

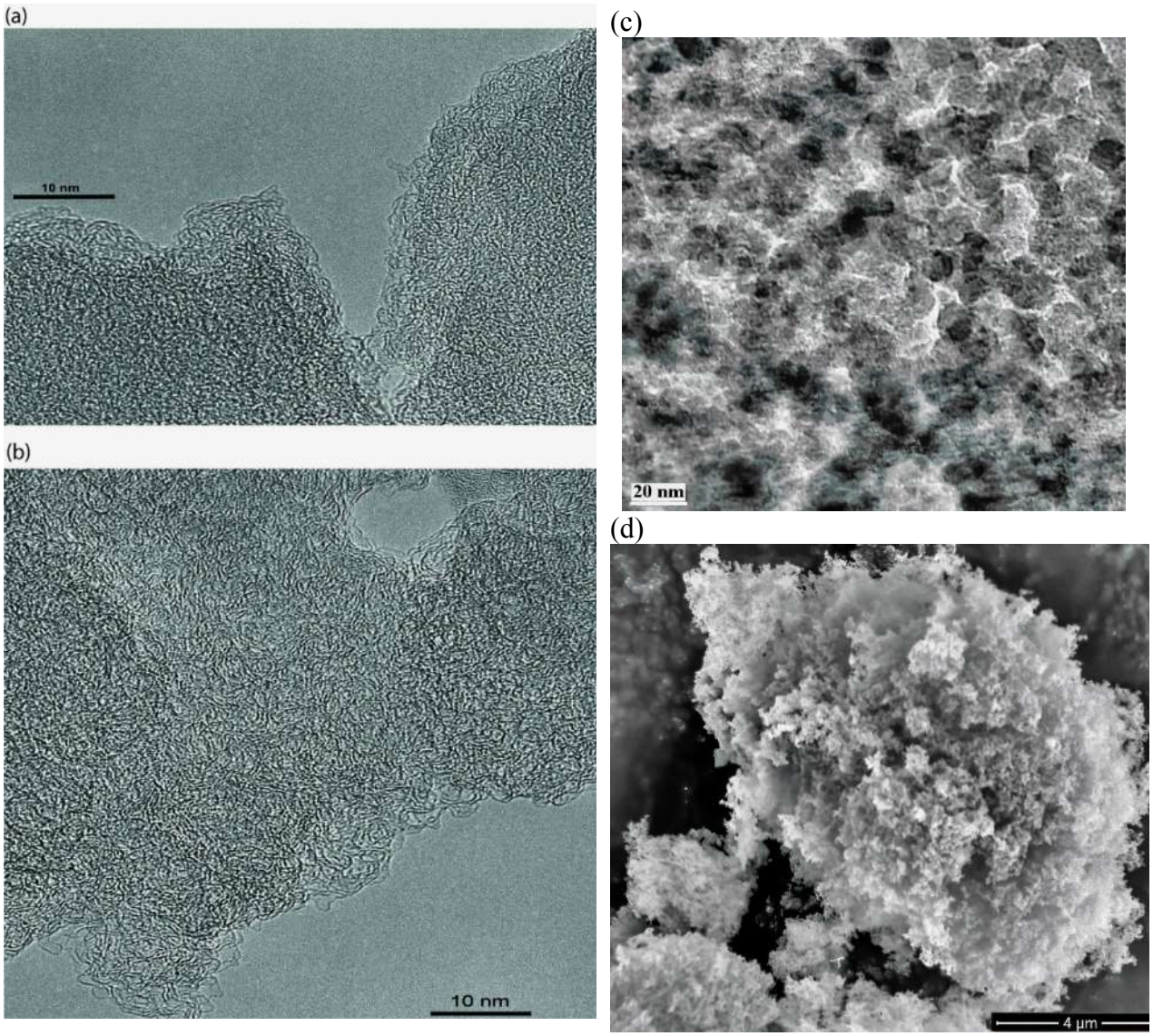

Fig. 2. TEM images of (a) char C–0, (b) AC C–50, (c) compacted A–300, and (d) SEM image of agglomerates in the initial A–300 powder

The texture and particular morphology of various adsorbents appear in the nitrogen adsorption-desorption isotherms (Fig. 5). For example, the main contribution of narrow pores in 200DF and MCM–41 leads to the shape of the nitrogen adsorption–desorption isotherms without or with very narrow hysteresis loop and almost plateau adsorption after $p/p_0 \approx$ 0.3–0.4 (Fig. 5, 200DF and MCM–41). Similar effects are observed for nanoporous AC (Fig. 5b, curves 3–6, and Fig. 4c),having mainly nanopores and a smaller contribution of narrow mesopores, or other materials with pore diameter smaller than 4 nm [1–16]. Note that pure or almost pure nanoporous AC (with $S_{nano}/S_{BET} > 0.95$) typically possess much smaller pore volume (Fig. 5b, curves 3 and 4, V_p) than AC with significant contribution of broad mesopores and macropores

(Table 1, *V*). The presence of broad meso/macropores (C–*x* series of AC) or very broad PSD (A–500) (Table 1, Figs. 6 and 7) leads to a significant hysteresis loop (AC, A–500) and the absence of the plateau adsorption (A–500).

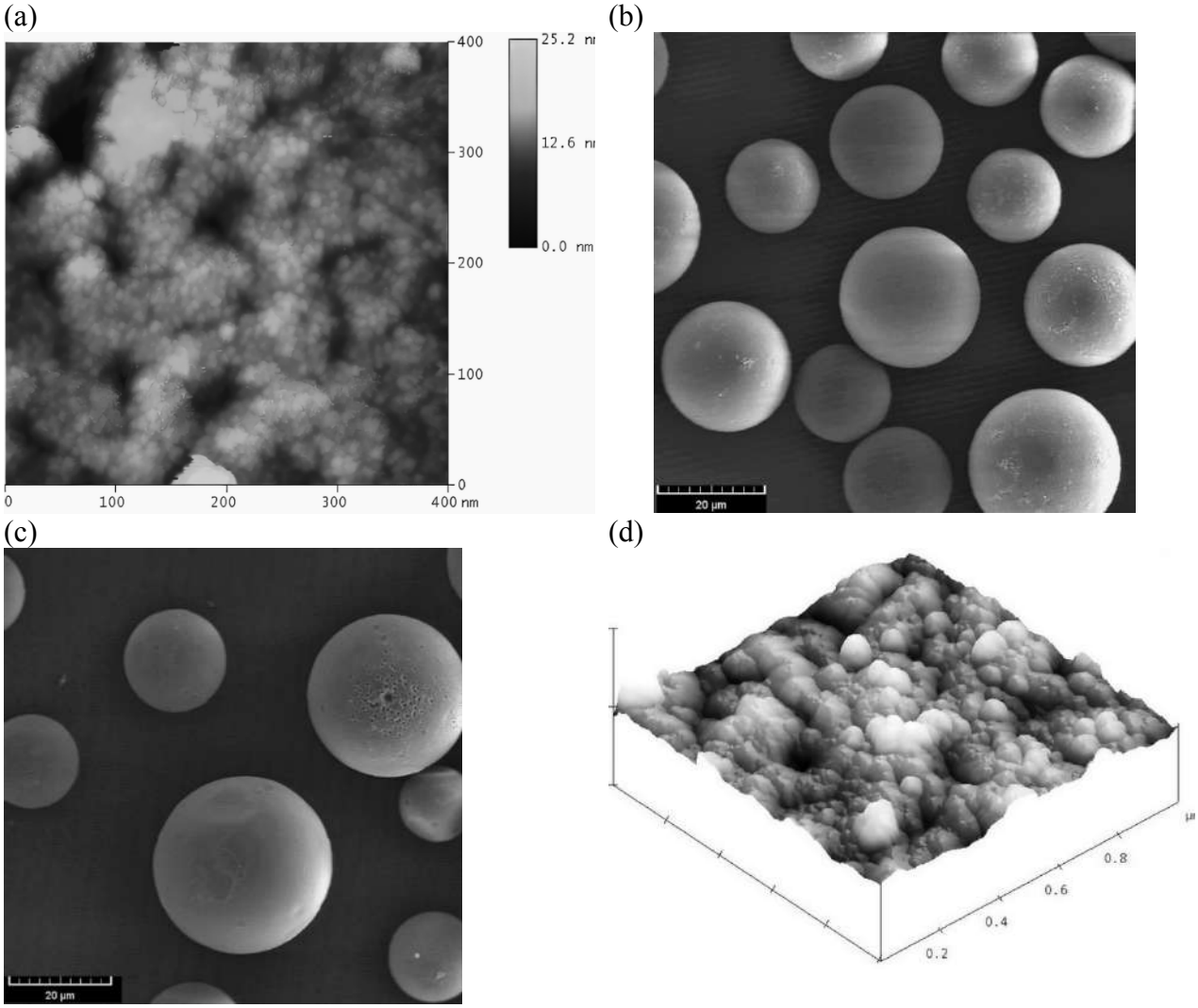

Fig. 3. AFM images of (a) C–30 and (d) A–300, and SEM images of microparticles of (b) C–0 and (c) C–30

Almost plateau adsorption for carbon adsorbents and later start of the hysteresis loop (Fig. 5) could be explained by the absence or a small contribution of narrow mesopores (Fig. 6c). This effect is smaller for SAXS PSD of C–0 (Figs. 4a and 6b) because SAXS 'sees' both open and closed pores. An increase in the burn-off degree of AC weakly affects the absence of pores of 1.5–3.0 nm in half width (Fig. 4b). As a whole, the burn-off effect for pores accessible for nitrogen molecules is significant (Figs. 4 and 5). Essential contributions of broader mesopores (5 nm $<R<$ 25 nm) and macropores($R>$ 25 nm) (Table 1, Figs. 4, 6, and 7) lead to the appearance of the hysteresis loops in the isotherms at $p/p_0>$ 0.8 for C–*x* carbons (Fig. 5). However, for nanosilica, it appears at lower pressure (Fig. 5a) due to different PSD comparing to that of AC C–*x* (Figs. 4–7).

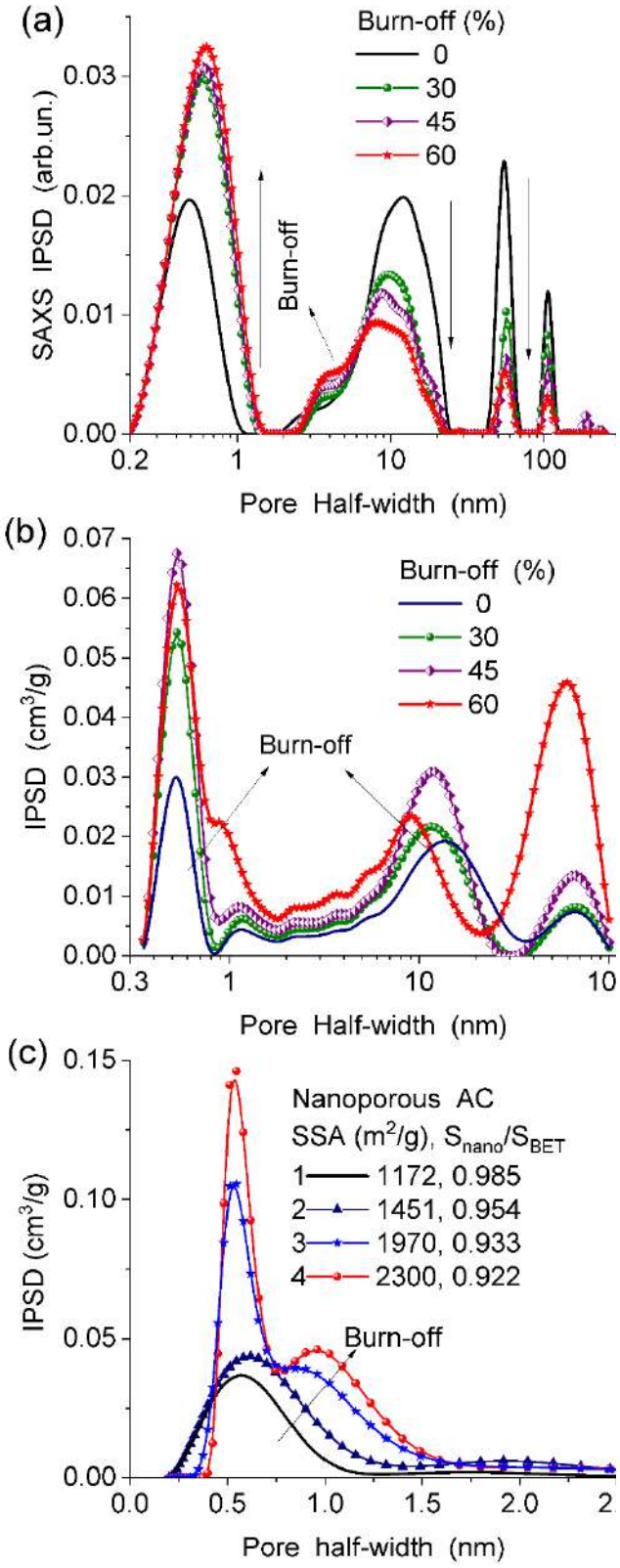

Fig. 4. PSD computed using (a) SAXS data and (b, c) nitrogen adsorption data for (b) char C–0 and AC with different burn-off degree (30, 45, and 60 %) and (c) nanopouous AC produced using raw natural precursors (DFT method)

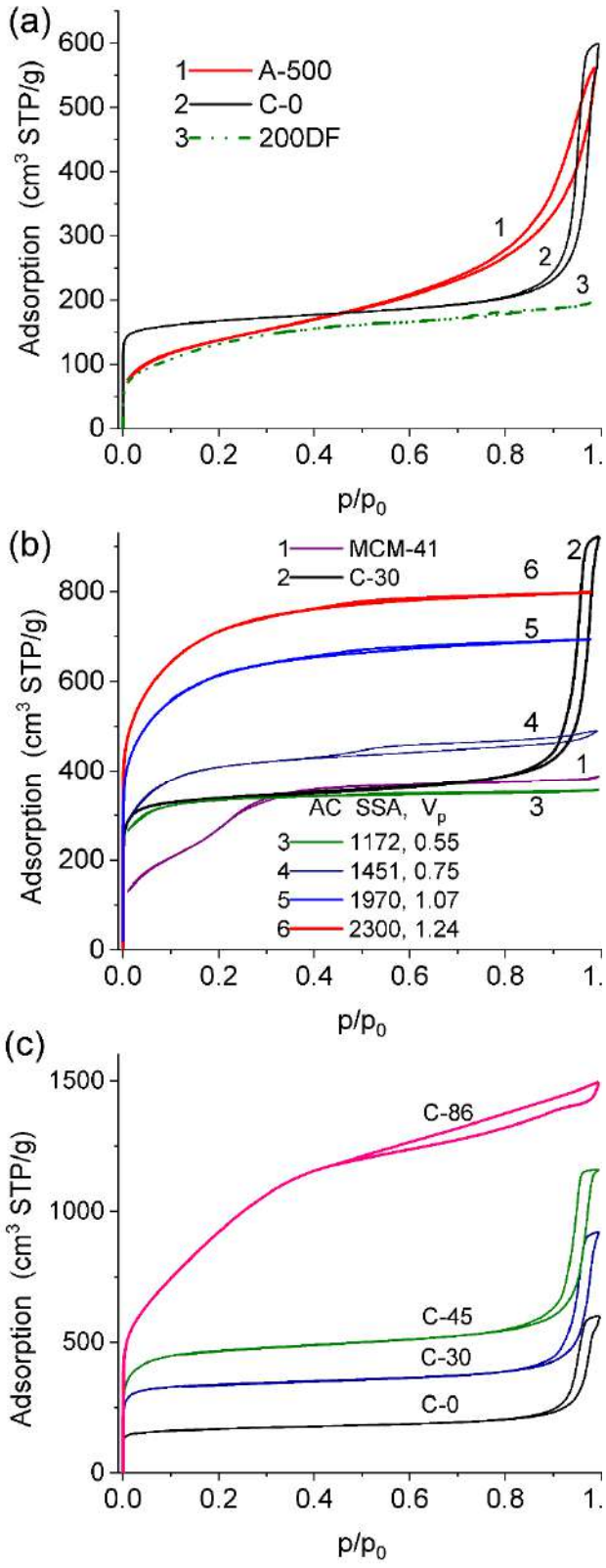

Fig. 5. Nitrogen adsorption–desorption isotherms for various silicas (a) A–500, 200DF, (b) MCM–41 and carbons (a) C–0, (b) C–30, and (c) C–0, C–30, C–45, and C–86; (b) nanoporous AC (curves 3–6)

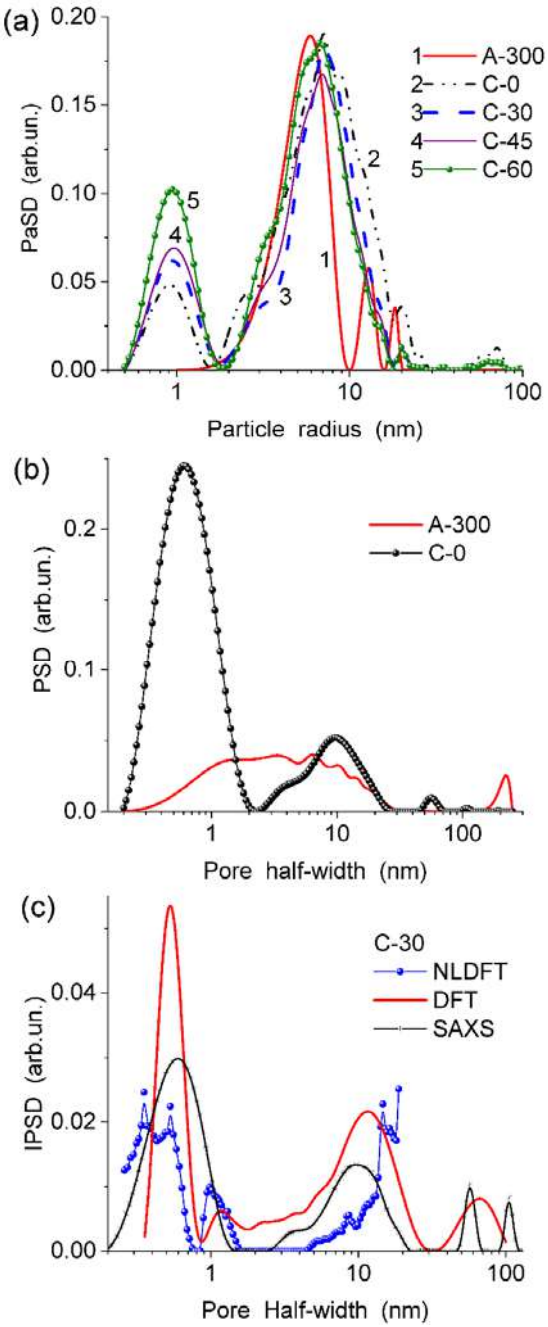

Fig. 6. (a) Particle size distributions and (b, c) PSD computed using (a–c) SAXS and (c) adsorption data

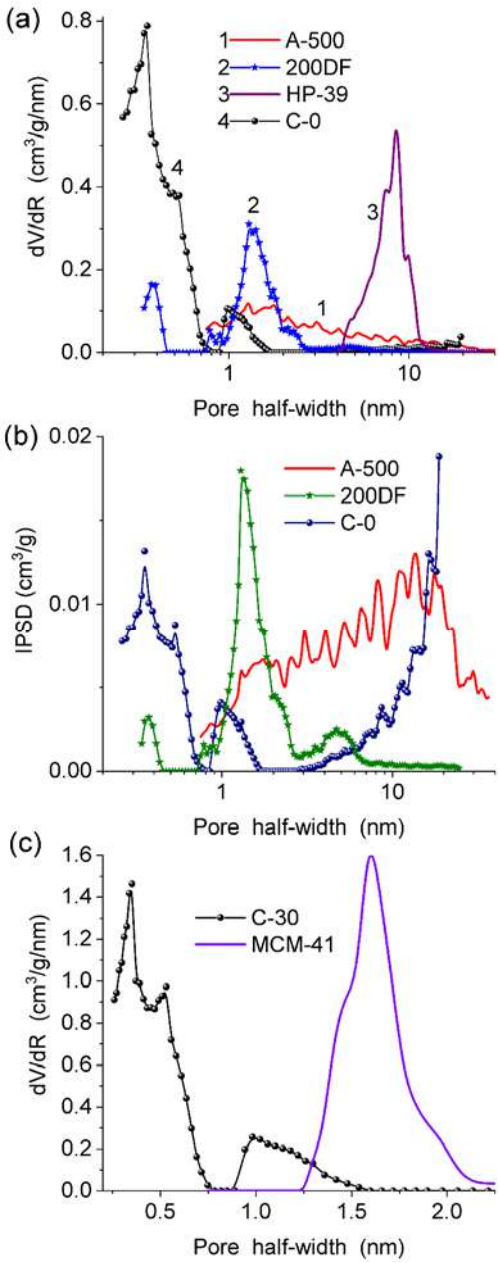

Fig. 7. (a, c) Differential and (b) incremental pore size distributions computed with the NLDFT method

Table 2. Relationship between the S_{SAXS} and S_{BET} values for some adsorbents

Sample	S_{SAXS} m^2/g	$(S_{SAXS}–S_{BET})/S_{SAXS}$
A–300	315	0.067
C–0	1194	0.550
C–30	2256	0.524
C–45	2175	0.257
C–60	2680	0.254

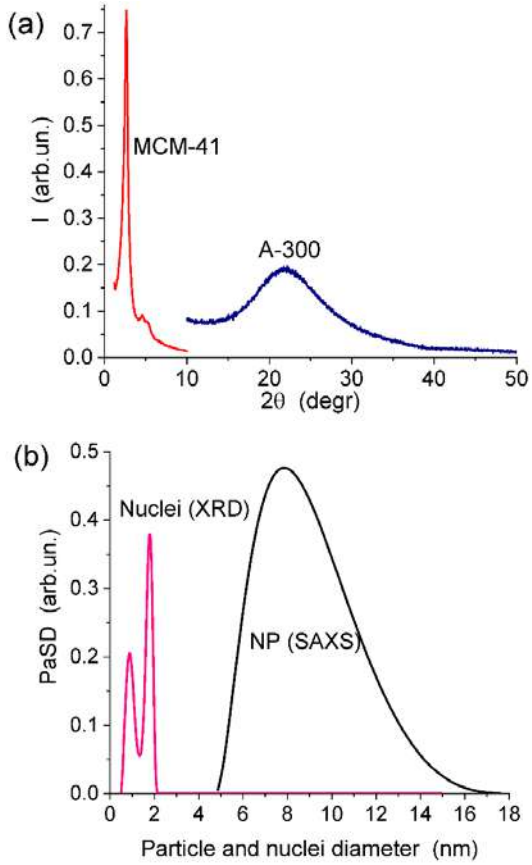

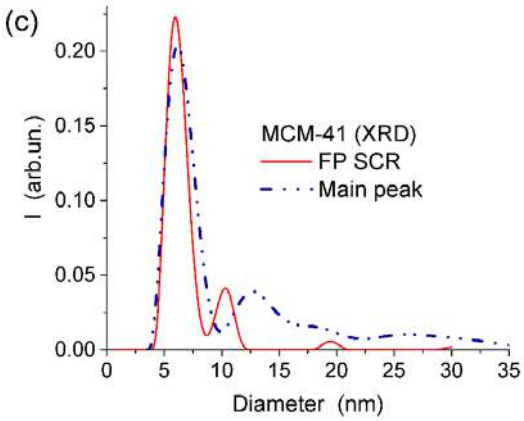

Fig. 8. (a) XRD patterns of A–300 and MCM–41, (b) size distributions of nuclei (XRD) and nanoparticles (SAXS) of A–300; and (c) size distributions of the coherent scattering regions for MCM–41 calculated using full profile (SCR procedure) and main XRD peak at 2.7°

(a)

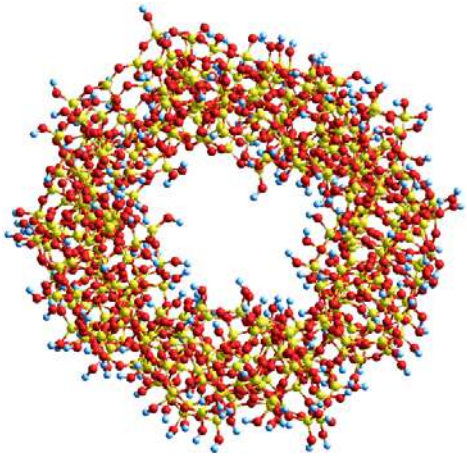

(b)

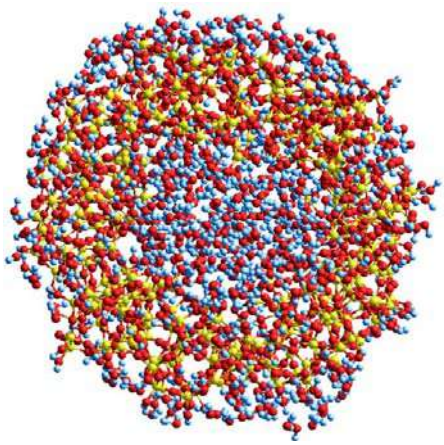

(c)

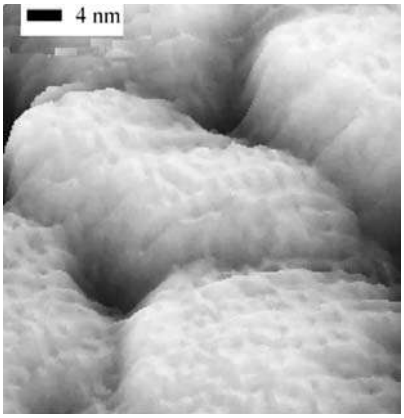

Fig. 9. Model of nanopore in silica (a) empty and (b) infilled by water, and (c) microscopic image of narrow pores in a silica adsorbent (details are in [16, 49])

MCM–41 is synthesized at much lower temperature (see details, *e.g.*, in [48]) than fumed silica; therefore, the nuclei registered in NP of fumed silica (Fig. 8b) are not observed in MCM–41 (Fig. 8c). The first peak of MCM–41 (Fig. 8c) corresponds to the coherent scattering region withone cell about $d_{XRD} + 2t_{wall}$ (Table 3). Other peaks (Fig. 8c) correspond to structures with two, three, or more cells of MCM–41. In the case of carbons C–*x*, SAXS PaSD (Fig. 6a) show the presence of small graphenes with 2–5 layers whose contribution increases with increasing burn-off degree. The main PaSD peaks of C–*x* are broader than that of A–300, which has the secondary PaSD peaks at *r* = 10–20 nm corresponding to primary aggregates of NPNP. Nanopores between small graphenes (Figs. 1, 2, and 6a) provide great SSA values for AC (Tables 1 and 2).

Even narrow pores (Fig. 7) in silica gel 200DF and ordered mesoporous silica MCM–41, as well as broader pores in silica gel HP–39 (Fig. 7a), correspond to pores in globules with tightly packed NP (Fig. 9) but not in NP *per se*i n contrast to char C–0 and AC C–*x*.

Table 3. Structural characteristics of MCM–41 calculated from the X-ray data.

Sample	d_{XRD} (nm)	d_{hkl} (nm)	d_{PSD} (nm)	t_{wall} (nm)
MCM–41	3.11	3.40	3.18	0.82

$d_{XRD} = 1.213 d_{100}\sqrt{\varepsilon}$ is the pore diameter, $\varepsilon = \rho_0 V_p / (1 + \rho_0 V_p)$; ρ_0 = 2.2 g/cm^3 is the true density of amorphous silicas; $d_{hkl} = \lambda / (2 \sin\theta_m)$ is the spacing value and θ_m is the angle corresponding to (hkl) reflection peak; $t_{wall} = a_0 - d_{XRD}$ is the thickness of pore walls and $a_0 = 2d_{100} / \sqrt{3}$ is the distance between pore centres; d_{PSD} is the pore diameter corresponding to the maximum in the NLDFT PDS (Fig. 7c) (see [48] for details).

Conclusion

The main difference in the textural characteristics of silica and carbon adsorbents is due to the absence (silicas) or presence (carbons) of nanopores in nanoparticles. A great contribution of these pores in strongly activated carbons (*e.g.*, C–60, C–86) provides the SSA values greater by an order of magnitude than that of fumed silicas. Despite a high activation degree of AC, contribution of closed pores or pores inaccessible for nitrogen molecules remains relatively large, *e.g.*, about 25% for C–60,but it is much smaller than that (55%) for char C–0. For fumed silica A–300, this contribution is small (about 7%) because nanoparticles were synthesized in the flame at high temperature (~80% of melting temperature for amorphous silica) with easy ‘cicatrization’ of small voids between nuclei in NP upon the hot synthesis. Therefore, the nanosilica pores inaccessible for nitrogen molecules could be attributed to narrow voids around contact area between neighboring NP in their aggregates that corresponds to the textural porosity characteristic for powders with NPNP.

For complete (nearly comprehensive) characterization of the morphology and texture of any adsorbents, TEM, SEM, adsorption, SAXS, and XRD methods could be used with appropriate software. The latter is especially important for the analyses of indirect data (*e.g.*, adsorption, SAXS, XRD). There is an additional aspect related to essential difference in conditions of measurements (*e.g.*, dried, degassed samples) and practical applications of the adsorbents (*e.g.*, in liquid dispersion media). Estimation of the characteristics for dried, degassed samples used then in liquid media can lead to certain errors if these characteristics are used to estimate the adsorbent efficiency in liquid media. In this case, some additional methods, *e.g.*, cryoporometry, relaxometry, thermoporometry, and confocal laser scanning microscopy [16] should be added to the mentioned above set of the methods.

There is an aspect of the adequacy and accuracy of used models of materialsstudied using the adsorption, SAXS and other methods. This problem is generated due to some restrictions of firm software linked to the corresponding equipment since the used models (including materials, equations, algorithms) could be inappropriate for the studied real materials (*e.g.*, a model of spherical particles for lamellar ones in SAXS, cylindrical pores for nanosilicas with complex voids between NPNP in the nitrogen adsorption, *etc*.). Therefore, developments of new programs with improved models, equations, and algorithms are of importance from a practical point of view.

Acknowledgements

The author is grateful to the National Research Foundation of Ukraine (Support of advanced and young scientists, grant 2020.02/0057) for financial support of the study. The author thanks Dr. O.I. Oranska, Dr. I. Protsak, and Prof. V.A. Tertykh (CISC), Dr. hab. B. Charmasand Dr. hab. J. Skubiszewska-Zięba(MCSU), and Dr. O.P. Kozynchenko (MAST Carbon International Ltd., UK) for some samples and experimental data.

References

1. Adamson A.W., Gast A.P. *Physical Chemistry of Surface. Sixth edition*. (New York: Wiley, 1997).
2. Gregg S.J., Sing K.S.W. *Adsorption, Surface Area and Porosity*. (London: Academic Press, 1982).
3. Thommes M., Kaneko K., Neimark A.V., Olivier J.P., Rodriguez-Reinoso F., Rouquerol J., Sing K.S.W. Physisorption of gases, with special reference to the evaluation of surface area and pore size distribution. IUPAC Technical Report. *Pure Application Chemistry.* 2015. **87**: 1051.
4. Gregg S.J., Sing K.S.W., Stoeckli H.F. (editors). *Characterization of Porous Solids*. (London: Soc. Chem. Industry, 1979).
5. Rouquerol J., Baron G.V., Denoyel R., Giesche H., Groen J., Klobes P., Levitz P., Neimark A.V., Rigby S., Skudas R., Sing K., Thommes M., Unger K. The characterization of macroporous solids: An overview of the methodology. *Microporous Mesoporous Mater*. 2012. **154:** 2.
6. ShegokarR.,Souto E.B. (editors), *Characterization of Micro and Nanoparticles for Biomedical Applications* (Micro and Nano Technologies). (Elsevier, 2024. ISBN: 9780323961387).
7. McEnaney B., Mays T.J., Rodriguez–Reinoso F. (editors). *Fundamental Aspects of Active Carbons*. Special issue. *Carbon* 1998. **36**(10).
8. Cooney D.O. *Activated Charcoal in Medical Applications*. (New York: Marcel Dekker, 1995).
9. Rodriguez-Reinoso F., McEnaney B., Rouquerol J., Unger K. (editors). *Studies in Surface Science and Catalysis, Vol. 144, Characterisation of Porous Solids VI*. (Amsterdam: Elsevier Science, 2002).
10. Biricik H., Sarier N. Comparative study of the characteristics of nano silica–, silica fume– and fly ash – incorporated cement mortars. *Materials Research.* 2014. **17**: 570.
11. Hashim A.A. (editor). *Smart Nanoparticles Technology*. (Rijeka, Croatia: InTech, 2012).
12. Iler R.K. *The Chemistry of Silica. Solubility, Polymerization, Colloid and Surface Properties, and Biochemistry*. (Chichester: Wiley, 1979).
13. Bergna H.E., Roberts W.O. (editors). *Colloidal Silica: Fundamentals and Applications*. (Boca Raton: CRC Press, 2006).

14. Legrand A.P. (editor). *The Surface Properties of Silicas*. (New York: Wiley, 1998).
15. *Basic characteristics of Aerosil fumed silica* (4th ed.). Tech. Bull. Fine Particles 11. (Hanau: Evonik Industries, 2014).
16. Gun'ko V.M., Turov V.V. *Nuclear Magnetic Resonance Studies of Interfacial Phenomena*. (Boca Raton: CRC Press, 2013).
17. Gun'ko V.M., Turov V.V., Zarko V.I., Goncharuk O.V., Pahklov E.M., Skubiszewska-Zięba J., Blitz J.P. Interfacial phenomena at a surface of individual and complex fumed Nanooxides. *Adv. Colloid Interface Sci*. 2016. **235**: 108.http://dx.doi.org/10.1016/j.cis.2016.06.003
18. Pietsch W. *Agglomeration in Industry*. (Weinheim: Wiley-VCH Verlag GmbH, 2005).
19. V.M. Gun'ko, V.V. Turov, O.V. Goncharuk, E.M. Pakhlov, O.K. Matkovsky, Interfacial phenomena at a surface of individual and complex fumed nanooxides.*Surface*.2019.**11(26):** 3.
20. Gun'ko V.M. Composite materials: textural characteristics. *Applied Surface Science*.2014. **307**: 444.
21. Gun'ko V.M., Morphological and textural features of various materials composed of porous or nonporous nanoparticles differently packed in secondary structures.*Applied Surface Science*.2021. **569**:151117.
22. Gun'ko V.M. Polymer adsorbents vs. functionalized oxides and carbons: particulate morphology and textural and surface characterization. *Polymers*.2021. **13**(8): 1249.
23. Gun'ko V.M., Meikle S.T., Kozynchenko O.P., Tennison S.R., Ehrburger-Dolle F., Morfin I., Mikhalovsky S.V. Comparative characterization of carbon and polymer adsorbents by SAXS and nitrogen adsorption methods. *J. Phys. Chem. C*. 2011. **115**: 10727.
24. Gun'ko V.M., Turov V.V., Kozynchenko O.P., Nikolaev V.G., Tennison S.R., Meikle S.T., Snezhkova E.A., Sidorenko A.S., Ehrburger-Dolle F., Morfin I., Klymchuk D.O., Mikhalovsky S.V. Activation and structural and adsorption features of activated carbons with highly developed micro-, meso- and microporosity. *Adsorption* 2011. **17**: 453.
25. Gun'ko V.M., Kozynchenko O.P., Tennison S.R., Leboda R., Skubiszewska-Zięba J., Mikhalovsky S.V. Comparative study of nanopores in activated carbons by HRTEM and adsorption methods. *Carbon*. 2012. **50**: 3146.
26. Gun'ko V.M. Nano/meso/macroporous materials characterization affected by experimental conditions and features of the used methods. *Chemistry, Physics and Technology of Surface*. 2020. **11**(1): 5.
27. Gun'ko V.M. Textural characteristics of composite adsorbents analyzed with density functional theory and self-consistent regularization procedure. *Chemistry, Physics and Technology of Surface*. 2020. **11**(2): 163.
28. Gun'ko V.M. Features of the morphology and texture of silica and carbon adsorbents.*Surface.* 2021.**13(28)**: 127.
29. Gun'koV.M.,Turov V.V. Particulate morphology and textural characteristics of nanosilica hydro-compacted at various wetting degree.*Chemistry, Physics and Technology of Surface*.2023. **14**: 3.
30. Tennison S.R. Phenolic resin derived activated carbons. *Appl. Cat. A Gen.* 1998. **173**: 289.
31. Tennison S.R., Kozynchenko O.P., Strelko V.V., Blackburn A.J. Porous carbons. US patent 2004024074A1, 2004.
32. Pujari P.K., Sen D., Amarendra G., Abhaya S., Pandey A.K., Dutta D., Mazubder S. Study of pore structure in grafted polymer membranes using slow positron beam and small-angle X-ray scattering techniques. *Nuclear. Instr. Method Phys. Res. B*. 2007. **254**: 278.

33. Sakurai S. SAXS evaluation of size distribution for nanoparticles. Chapter 5 (http://dx.doi.org/10.5772/105981). in A.E. Ares (editor). *X-rayScattering*. (DOI: 10.5772/65049). (RijekaCroatia: InTech, 2017, pp. 107-134).
34. Brumberger H. (editor). *Small Angle X-ray Scattering*. (New York: Gordon&Breach, 1965).
35. Dieudonné Ph., Hafidi A.A., Delord P., Phalippou J. Transformation of nanostructure of silica gels during drying. *J. Non-Crystal. Solid*. 2000. **262**: 155.
36. Fairén-Jiménez D., Carrasco-Marín F., Djurado D., Bley F., Ehrburger-Dolle F., Moreno-Castilla C. Surface area and microporosity of carbon aerogels from gas adsorption and small- and wide-angle X-ray scattering measurements. *J. Phys. Chem. B.*2006. **110**: 8681.
37. Provencher S.W. A constrained regularization method for inverting data represented by linear algebraic or integral equations. *Comp. Phys. Comm.* 1982. **27**: 213.
38. Cullity B.D., Stock S.R. *Elements of X-Ray Diffraction*. Third Edition. (New York: Prentice-Hall Inc., 2001).
39. Guinier A. *X-Ray Diffraction.* (San Francisco: WH Freeman, 1963).
40. de Avillez R.R., Abrantes F.G., Letichevsky S. On the intrinsic limits of the convolution method to obtain thecrystallite size distribution from nanopowders diffraction. *Mater. Res*. 2018. **21**(3): e20170980.
41. Popović S., Skoko Ž. X-ray diffraction broadening analysis. *Maced. J. Chem. Chem. Eng.* 2015. **34**(1): 39.
42. Gun'ko V.M., Oranska O.I., Paientko V.V., SulymI.Ya. Particulate morphology of nanostructured materials. *Chemistry, Physics and Technology of Surface*. 2020. **11**: 368.
43. A.V. Neimark, P.I. Ravikovitch, Capillary condensation in MMS and pore structure characterization, *Micropor.Mesopor. Mater*. 2001.**44**/**45**: 697.
44. Ravikovitch P.I., Neimark A.V. Density functional theory model of adsorption on amorphous and microporous silica materials. *Langmuir.*2006. **22**: 11171.
45. Landers J., Gor G.Y., Neimark A.V. Density functional theory methods for characterization of porous materials. *Colloids Surf. A: Physicochem. Eng. Aspects.* 2013. **437**: 3.
46. Neimark A.V., Lin Y., Ravikovitch P.I., Thommes M. Quenched solid density functional theory and pore size analysis of micro-mesoporous carbons. *Carbon*. 2009. **47**: 1617.
47. Gor G.Y., Thommes M., Cychosz K.A., Neimark A.V. Quenched solid density functional theory method for characterization of mesoporous carbons by nitrogen adsorption. *Carbon*. 2012. **50**: 1583.
48. Gun'ko V.M., Turov V.V., Turov A.V., Zarko V.I., Gerda V.I., Yanishpolskii V.V., Berezovska I.S., Tertykh V.A. Behaviour of pure water and water mixture with benzene or chloroform adsorbed onto ordered mesoporous silicas.*Central European Journal of Chemistry.* 2007, **5**: 420.
49. Gun'ko V.M., Turov V.V., Gorbik P.P. *Water at the Interfaces*. (Kyiv: Naukova Dumka, 2009).

ОСОБЛИВОСТІ ПОРИСТОСТІ ТА ПАКУВАННЯ НАНО- ТА МІКРО-ЧАСТИНОК ВУГЛЕЦЕВИХ ТА КРЕМНЕЗЕМНИХ АДСОРБЕНТІВ

В.М. Гунько
Інститут хімії поверхні ім. О.О. Чуйка Національної академії наук України
вул. Генерала Наумова, 17, Київ, 03164, Україна,
e-mail:vlad_gunko@ukr.net

Порівняльна характеристика морфології частинок і текстури різних діоксидів кремнію (пірогеневі діоксиди кремнію, силікагелі, впорядковані мезопористі діоксиди кремнію) і вуглецевих матеріалів (кабонізат та активоване вугілля, АС) становить інтерес як з теоретичної, так і з практичної точок зору, оскільки це дозволяє краще зрозуміти переваги та недоліки різних адсорбентів при застосуванні для різних адсорбатів у різних дисперсійних середовищах. Повна характеристика адсорбентів потребує застосування певного набору методів, який аналізується в цій статті. Показано, що основна відмінність у текстурних характеристиках кремнеземних і вуглецевих адсорбентів зумовлена відсутністю (кремнеземи) або наявністю (вуглеці) нанопор у наночастинках (НЧ). Великий внесок цих пор у сильно активоване вугілля забезпечує значення питомої поверхні на порядок більші, ніж у нанокремнеземів. Незважаючи на високий ступінь активації АС, внесок закритих пор або пор, недоступних для молекул азоту, залишається відносно великим на відміну від пірогенного кремнезему А-300, що складається з наночастинок, синтезованих у полум'ї при вищій температурі (~80% температури плавлення, T_m, для аморфного кремнезему), ніж температура активації вуглецю (~25% T_m для вуглецю). Таким чином, пори, недоступні для молекул азоту в пірогенному кремнеземі, можна віднести до вузьких порожнеч навколо контактної зони між сусідніми наночастинками в їхніх агрегатах, але для АС існують як закриті пори, так і відкриті пори, недоступні для молекул азоту. Для повної характеристики морфології та текстури різних адсорбентів може використовуватися набір методів, таких як трансмісійна і скануюча електронна мікроскопія, зондова адсорбція (азот, аргон), малокутове розсіювання рентгенівських променів (МКРРП)та рентгенофазовий аналіз (РФА),які треба використовувати з відповідним програмним забезпеченням. Останнє особливо важливо для аналізу непрямих даних (наприклад, адсорбція, МКРРП, РФА).

Ключові слова: *пірогенний кремнезем; пористі кремнеземи; вуглецеві адсорбенти; морфологія частинок; пористість наночастинок; структурно-адсорбційні характеристики*